Backprojection analyses from four regional arrays for rupture over a curved dipping fault: The M_w 7.7 24 September 2013 Pakistan earthquake

Dun Wang[1], Hitoshi Kawakatsu[1], Jim Mori[2], Babar Ali[3], Zhikun Ren[4], and Xuelin Shen[5]

[1]Earthquake Research Institute, University of Tokyo, Tokyo, Japan, [2]Disaster Prevention Research Institute, Kyoto University, Uji, Japan, [3]Pakistan Metrological Department, Islamabad, Pakistan, [4]State Key Laboratory of Earthquake Dynamics, Institute of Geology, China Earthquake Administration, Beijing, China, [5]Institute of Seismology, China Earthquake Administration, Wuhan, China

Abstract We analyzed the 24 September 2013 Pakistan earthquake (M_w 7.7) with backprojection analyses using data recorded on four different regional arrays in Europe, China, and Japan (Hi-net and F-net). The results from all the arrays show propagation of the rupture toward the southwest for duration of about 40–50 s. Among them, results for Hi-net and a subset of China array show a clear segment of fast rupture propagation, with a rupture speed probably faster than the local shear wave velocity. Resolutions of the results from the various arrays are investigated using bootstrap tests, backprojection of aftershocks, and numerical tests with synthetic source models. The results of those tests show differences in the quality of the results from the four arrays. The China array and the Hi-net in Japan show the best results for this case. F-net in Japan shows the poorest results because of the few number of stations. The locations of large amplitudes (equivalent to a M 6.8 event) have absolute uncertainties of about 20 to 30 km (ignoring the source dimension).

1. Introduction

On 24 September 2013, a M_w 7.7 earthquake (65.500°N, 26.951°E, depth: 15.0 km, from U.S. Geological Survey (USGS)), occurred along the curved southern segment of the Chaman Fault System, in the region of the junction of the Arabian, Eurasian, and Indian plates. It caused at least 825 deaths in the province of Balochistan, Pakistan, and a small tsunami with maximum height of ~1 m (caused by a submarine landslide) at Qurayat, Oman [*Heidarzadeh and Satake*, 2014]. The Chaman Fault System is a part of the Eurasian-India plate boundary [*Byrne et al.*, 1992]. The northward motion of the India Plate drives left-lateral strike-slip displacement along the northern Chaman Fault, as well as the eastern Makran folds, which are dragged northeastward along the southern Chaman Fault. The Chaman Fault System has long been observed to be a transform zone between strike-slip and thrust faulting, connecting the Himalayan and Makran convergence zones from north to south [*Lawrence et al.*, 1981]. Previous studies demonstrated that a slip potential of 4 m has been accumulated along the northern Chaman Fault System during the last century [*Ambraseys and Bilham*, 2003].

Horizontal surface displacements caused by the earthquake were measured by optical images, revealing a 180–200 km long continuous surface break out [*Avouac et al.*, 2014; *Barnhart et al.*, 2014; *Jolivet et al.*, 2014; *Yague-Martinez et al.*, 2014; *Zinke et al.*, 2014]. The north, fault-parallel displacement pattern suggests that the earthquake nucleated on a subvertical segment and then ruptured along a 50° north dipping fault [*Jolivet et al.*, 2014]. The fault slip is mainly concentrated in the top 10 km with no significant displacement on the underlying décollement [*Jolivet et al.*, 2014]. The aftershocks mainly occurred north of the source area, while even early backprojection results (for example, in ds.iris.edu/spud/backprojection) showed the opposite direction of the rupture propagation. An interesting phenomenon is the scarcity of aftershocks in the southwest extension of the source area (Figure 1) where the surface deformation and seismic radiation (damages) were the largest [*Avouac et al.*, 2014; *Barnhart et al.*, 2014; *Jolivet et al.*, 2014; *Yague-Martinez et al.*, 2014; *Zinke et al.*, 2014].

In this study we use a backprojection method with data from four independent arrays to study the high-frequency energy release for the earthquake. Backprojection analysis has become one of the common approaches to delineate the earthquake rupture pattern for large earthquakes [*Ishii et al.*, 2005; *Kruger and Ohrnberger*, 2005; *Ishii*, 2011; *Koper et al.*, 2012; *Yao et al.*, 2012; *Kennett et al.*, 2014]. Backprojecting data recorded on large regional arrays have shown many rupture details for complex rupture patterns
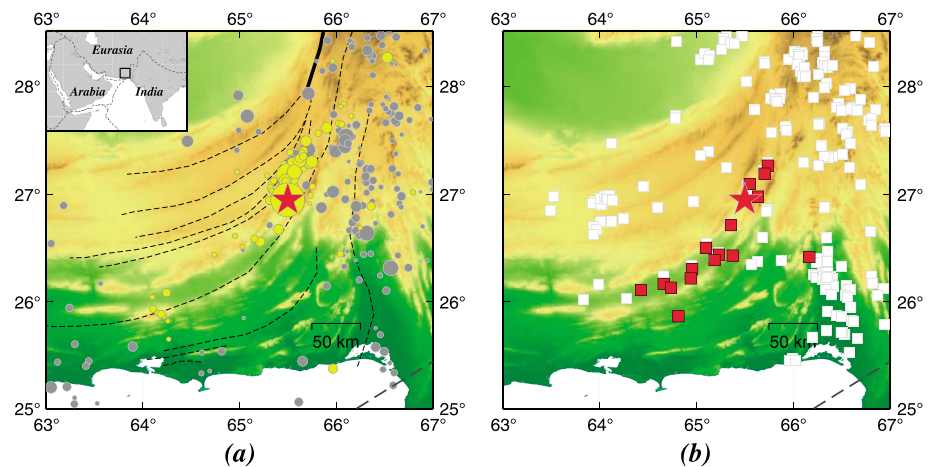
Figure 1. (a) Locations of aftershocks (yellow circles) that occurred within 1 week following the main shock and previous seismicity (gray circles). Black solid and dashed lines indicate surface traces of known faults [*Lawrence et al.*, 1981]. The red star indicates the epicenter determined by the USGS. (b) White and red shaded squares indicate health facilities which were undamaged and damaged, respectively (http://www.ndma.gov.pk).

(for example, the 2012 *M* 8.6 Off-Sumatra earthquake [*Meng et al.*, 2012; *Satriano et al.*, 2012; *Wang et al.*, 2012; *Yue et al.*, 2012; *Ishii et al.*, 2013]).

With a shifted epicenter, a backprojection study based on Hi-net data showed similar rupture patterns, and a rupture speed of 3.0 km/s with segments of possible supershear ruptures for the 2013 Pakistan earthquake [*Avouac et al.*, 2014]. In order to further investigate the rupture details and the reliability of the backprojection method, we compare results and carry out several resolution tests using regional networks in Europe, China, and Japan. Using data recorded in several frequency bands at four independent arrays, we investigate the initiation points, rupture length, rupture speed, and the associated uncertainties of the results.

2. Backprojection Analysis With Multiple Seismic Arrays

2.1. Data

We use data recorded on large arrays in Europe, China, and Japan (F-net and Hi-net) (Figure 2).

The European regional array (http://eida.gfz-potsdam.de/webdc3/) is a combined network of more than 350 broadband stations consisting of more than 50 network operators. The epicenter distances to the Pakistan earthquake range from 28° to 62° with azimuths of 287° to 324°. Many of the stations are located close to the west-northwest striking nodal plane.

The China array (http://www.ceic.ac.cn/) is another large regional seismic network, with over 800 broadband seismic stations. The stations are denser in the south and in other earthquake-prone areas such as the Huabei earthquake belt. The epicenter distances are from 30° to 49.5° with azimuths of 43° to 89°.

The Hi-net array (http://www.hinet.bosai.go.jp) in Japan consists of ~770 evenly distributed borehole stations with short-period seismometers spread over an area of about 378,000 km^2 [*Okada et al.*, 2004]. Also in Japan, the F-net array (http://www.hinet.bosai.go.jp) consists of ~80 evenly distributed stations over Japan islands with broadband seismometers installed on the surface. The epicenter distances to Japanese arrays range from 55° to 65° with azimuths of 51° to 78°.

2.2. Method

The backprojection method uses waveforms from array data to determine the location of a source that is most consistent with relative timing of the arrival of the seismic waves. For teleseismic distance (distance of 30° to 90°), usually the direct *P* arrival is used. Similar to *Kruger and Ohrnberger* [2005], we perform the beamforming over a sliding/moving window offset by 1 s to image the stacked energy corresponding to each grid point [*Wang et al.*, 2016]. Since the obtained time is the local beam time, a time correction to account for the directivity effect in time is necessary because of the varying locations of the seismic sources
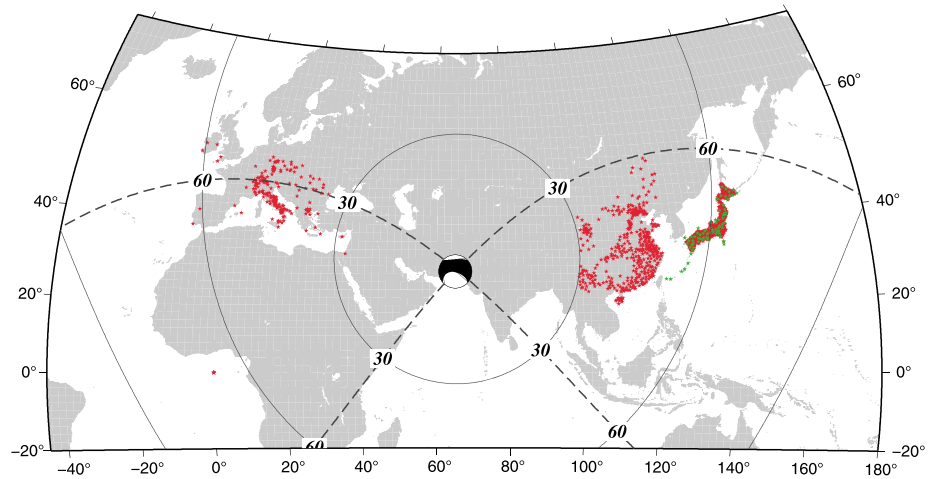
Figure 2. Station map for the European regional array (left, red), China array (middle, red), and F-net (right, green) and Hi-net (right, red) array in Japan. The focal mechanism is determined by the GCMT. Solid and dashed lines show the epicenter distances and strikes of the fault planes, respectively.

[*Kruger and Ohrnberger*, 2005]. Notice that conventional backprojection [e.g., *Ishii et al.*, 2005] does not require a time correction for directivity effect.

In this paper, the backprojection procedure consists of the following steps:

1. Set up grid of 71×41 points at a depth of 15 km with spacing of 5 km and strike of 230° over the source area.
2. Filter (0.5 to 2.0 Hz, 0.8 to 8.0 Hz, and 1.0 to 10.0 Hz) and align waveforms by cross correlation using a window length of 10 s to calculate station corrections.
3. Calculate travel times from each grid point to stations [*Kennett and Engdahl*, 1991].
4. Apply the theoretical travel times and station corrections and stack the waveforms for a window length of 10 s. For the stack amplitude, we use the square of the summed amplitudes [*Wang and Mori*, 2011a].
5. Shift the time window 1 s and calculate the stack amplitude. Repeat steps 3–5 for 100 time windows. The first window (time zero in the results such as in Figure 3, bottom row) is set 5 s before and after the *P* onset at the reference station.
6. Apply a time correction for the directivity effect caused by the progressive change in source position [*Kruger and Ohrnberger*, 2005; *Yao et al.*, 2011; *Wang et al.*, 2016].

Since we use station corrections (step 2), the backprojection is done for times relative to the initial arrival, and we need to assume the initial epicenter. At first we use the USGS epicenter and then modify this later in the paper. For the station corrections, we calculate cross correlations with a model waveform that is recorded at the center of the array; we discard stations that have correlation coefficients less than 0.4 for the filtered waveforms. The total numbers of stations used for the backprojections are 196–256 for the European array, 241–267 for the Chinese array, 69–74 for the F-net, and 608–741 for the Hi-net. The station correction helps in compensating for structure heterogeneities beneath the stations that affect travel times. Example of the data processing is shown in Figure S1 in the supporting information.

Because we use times relative to the initial arrival of *P* wave, we need to make a time correction to obtain the correct timing (step 6). For an array located in the same/opposite direction as the rupture propagation, the apparent time will be shortened/lengthened due to the directivity effect [*Kruger and Ohrnberger*, 2005; *Ni et al.*, 2005; *Yao et al.*, 2011]. The time corrections are then calculated following *Yao et al.* [2011].

In this study we carried out the backprojection analyses for three different frequency bands of 0.5 to 2.0 Hz, 0.8 to 8.0 Hz, and 1.0 to 10.0 Hz, although the vast majority of coherent energy being imaged in this processing is closer to 1–2 Hz. The lower frequencies tend to have poorer resolution in space and time because the waveforms become very similar in shape. The higher frequencies can resolve more details of the rupture propagation; however, the waveforms will lose the coherency. From past experience of looking at a wide range of frequencies from various earthquakes, these three frequency ranges give the best results. Identifying common features in all three frequency bands, one can increase the reliability in the interpretation of the results, although it
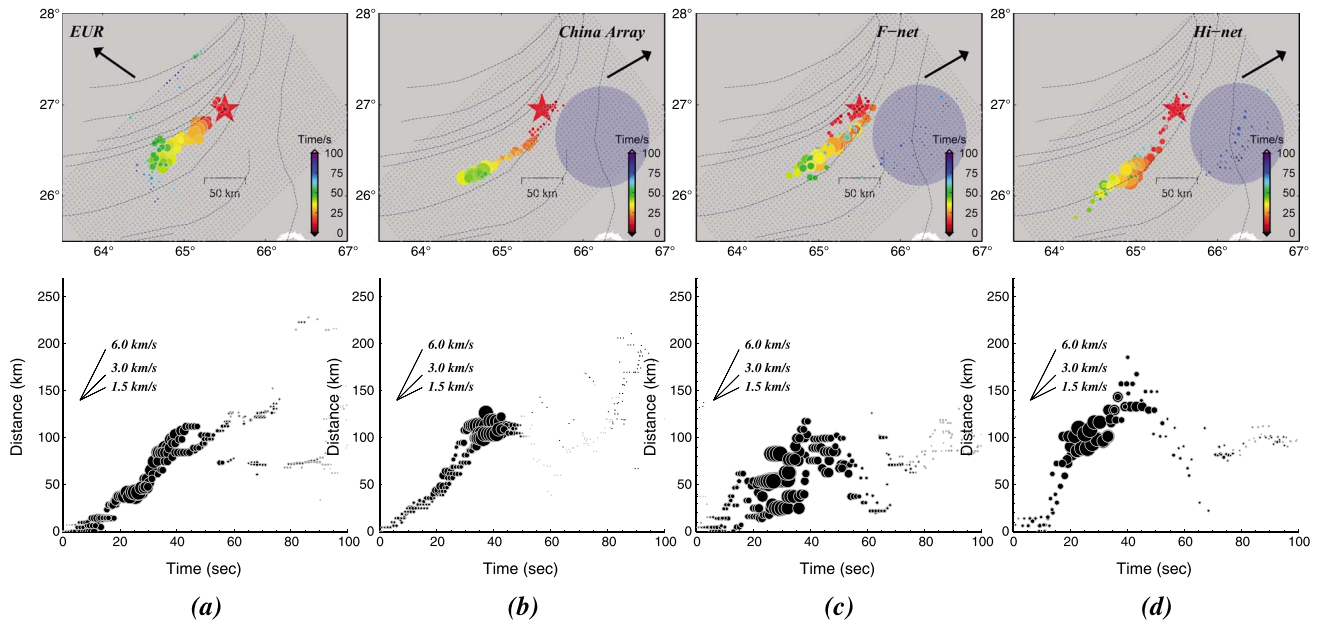
Figure 3. Timing (color of circles) and amplitude (size of circles) for the stack with the maximum correlation at each time step (1 s) (top row) in the map view and (bottom row) in time-distance plots in three frequency bands (between 0.5 and 2.0 Hz, 0.8 and 8.0 Hz, and 1.0 and 10.0 Hz). Distance is measured in a straight line from the epicenter. Results for (a–d) four arrays in Europe, China, and Japan are shown. Transparent blue circle indicates the locations of another possible source (aftershocks) 60–100 s after origin time.

is complicated by the fact that there are often strong frequency-dependent differences seen in the backprojection results [e.g., *Ishii*, 2011; *Kiser and Ishii*, 2011; *Wang and Mori*, 2011b; *Koper et al.*, 2012; *Yao et al.*, 2013].
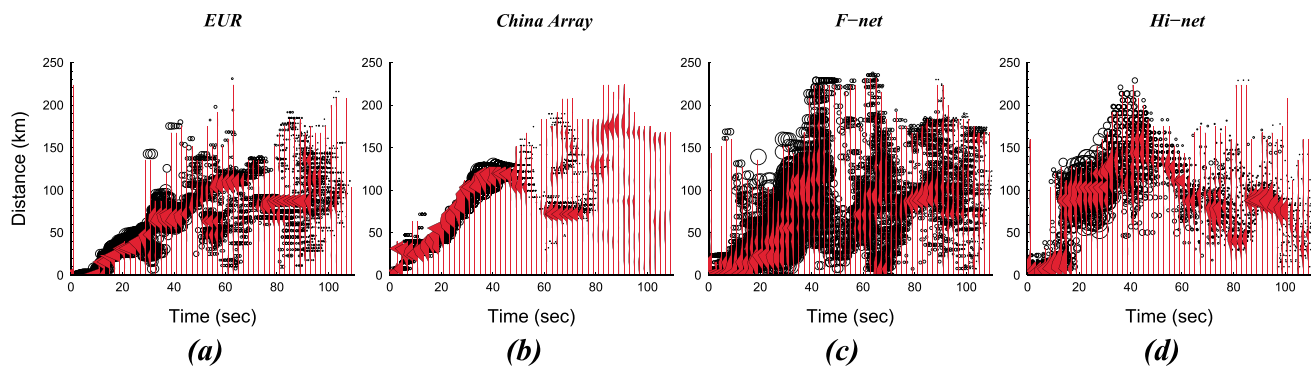
2.3. Results

The backprojection results for the four different arrays are shown by the locations of the maximum stack amplitude for each time window (Figure 3, top row) and the associated distances from the epicenter (Figure 3, bottom row). The determined locations of the relatively high frequency sources shown in Figure 3 are inferred to be the locations of rupture front of the earthquake, since the rupture front is expected to radiate more high-frequency [e.g., *Spudich and Frazer*, 1984; *Ide*, 2002; *Kiser and Ishii*, 2011]. In the map view in Figure 3 (top row), all four arrays show the general southwest propagation for the earthquake for about 40–50 s of rupture. Looking in more detail, the rupture propagates toward the southwest for the first 20 s and then moves in a more west-southwest direction for the next 20 to 30 s. In the time-distance plots in Figure 3 (bottom row), the largest amplitude occurs at 20 to 50 s after the initiation. There are some small amplitude arrivals from 60 to 100 s that seem fairly consistent among the various arrays, but they are not on the trend of the southwest propagation. There are likely early aftershocks that occur at locations on and off the main fault.

There are some significant differences between the results from the different arrays. The results for F-net in Japan, especially the time-distance plot, show considerable scatter, which is probably due to the small number of stations used. Also, the length of the rupture seems to vary between the different arrays, with the European array, China array, and F-net showing a rupture length of about 100 to 130 km, while Hi-net showing a longer rupture of about 150 to 180 km (see also in Movie S1). For the time-distance plots of Figure 3 (bottom row), the slopes of the trends show the propagation speed. Since the distances are measured in a straight line from the epicenter, these are lower bounds. For the broadband data from Europe, China, and F-net, we see rupture speeds of about 3.0 km/s; however, the Hi-net data show very fast speed of 4.0 to 5.0 km/s, which is faster than the local S wave velocity of 3.6 to 3.7 km/s at depth of 12 to 26 km [e.g., *Laske et al.*, 2001].

3. Resolution Tests

3.1. Bootstrap Test

To investigate the reliability of the backprojection results, we applied the bootstrap method [*Efron*, 1979], in which we randomly resample the stations used for the procedure (the total number of stations is the same,

Figure 4. Time-distantance plots for results of bootstrap analysis. Black circles represent maximum stacked amplitude points for 100 resampled data sets for each array. Vertical red lines with shaded upper areas are histograms of the stacked amplitude points for each time step, so areas of the red show regions of many consistent values.

but the random resampling allows choosing the same station multiple times). Waveforms are filtered between 1.0 and 10.0 Hz. We repeat this calculation 100 times for each array. The resampled stations are equally weighted. Figure 4 shows the 100 results of the bootstrap test for each time window (open circles) on the time-distance plots. Also, the vertical red lines (with filled upper portions) are histograms showing where there are many similar values. Results derived from the China and Hi-net data show less scatter (especially for the China data) compared to those obtained from Europe and F-net. The poorer resolution for F-net can be probably attributed to the fewer number of stations. Although the takeoff angles are close to one of the nodal planes of the focal mechanism for the European array, we do not observe large scattering from this test. Small-amplitude nodal arrivals can be affected more by local structure which would decrease the similarity among the waveforms.

One interesting point from these tests is that for all the arrays except European array, there are fairly stable locations of the sources from 60 to 80 s at a distance of about 70 km. These features are located far to the east of the fault in Figure 3.

3.2. Backprojection of Small Earthquakes

In order to evaluate the possible location bias from arrays in different azimuths and with different local structure along the path, we perform backprojections using data recorded in Europe and Japan for four aftershocks with magnitude range from 5.5 to 6.8 (Table 1). We use station corrections derived from the main shock and apply to these aftershocks to investigate the uncertainty of the backprojection locations for areas apart from the main shock epicenter. The epicenters determined by the USGS are used.

For the relatively small earthquakes, the M 5.5 and 5.6 earthquakes, the local maximum is rather scattered over the grid area that is larger than the expected source size, especially for the smaller amplitudes. Also, there is a clear bias in the directions of the recording arrays (Figure 5). This is the so-called "swimming artifact" [*Koper et al.*, 2012]. Results for the M 6.8 earthquake show more concentrated locations of the source points, with locations that are likely consistent with the centroid where the majority of moment is released. The smaller amplitudes still show a bias in the direction of the array. A northeast offset of about 20 km between the locations of the maximum stacked points and the epicenter is seen for all array results, and it might represent the location uncertainty or/and the finite extension of the source dimension.

This test indicates that backprojection results from the three arrays should have good resolution if the amplitudes are equivalent to a M 6.8 earthquake, which would correspond to amplitude of about one tenth to one eighth of the maximum amplitudes in the P wave of the Pakistan main shock. The resolution of the locations for the larger amplitudes is probably about 20 to 30 km.

3.3. Numerical Tests

We perform several numerical tests to evaluate the station and source geometry for resolving the rupture locations and speed. We generate synthetic waveforms for the case of the Pakistan main shock recorded on the four arrays. Synthetic seismograms including teleseismic P, pP, and sP are calculated using the program of Kikuchi and Kanamori (http://www.eri.u-tokyo.ac.jp/ETAL/KIKUCHI/, 2006) using eight point sources

Table 1. Detailed Information for the Small Earthquakes That Are Used for Resolution Test in the Main Text (USGS)

Time	Latitude	Longitude	Depth (km)	Mag Type	Magnitude	Catalog
2013-09-28 T07:34:06	27.1825	65.5052	12	M_w	6.8	USGS
2013-09-24 T17:20:13	27.1310	65.4710	10.5	Mb	5.5	USGS
2013-09-24 T13:01:39	27.3125	65.6201	14.5	Mb	5.6	USGS
2013-09-24 T11:36:27	27.2085	65.5674	10	Mb	5.8	USGS

with varying moments that are spaced at a 30 km interval along the fault line with strike-slip focal mechanisms. Since the earthquake had variable strike and dip for the fault [e.g., *Avouac et al.*, 2014], the first three point sources have strike = 190°, dip = 87°, slip = −10°, and the later five sources have strike = 228°, dip = 46°, slip = −10°. The strike-slip mechanisms produce relatively small amplitude direct *P* waves and larger depth phases. A triangle shape source time function with half width of 1 s and moment of $1 - 4 \times 10^{18}$ Nm are set for each point source. Notice that here the sampling interval for the European data is 0.05 s and is 0.01 s for the other arrays. Since the seismograms are normalized by amplitude in the backprojection procedure, the absolute size of the subevents becomes less important in this test. The tested scenario has a rupture that starts with a speed of 1.5 km/s for the first 60 km and then jumps to 5.0 km/s for the remaining rupture. Here the correct epicenter location is used for calculating the station corrections. The depths of the seven sources are set at 17, 29, 11, 23, 5, 17, 29, and 11 km, respectively.

We first evaluate the effect of the background noise level using Hi-net data. For the noise, we used a typical early morning period (15 November 2013 05:25:00 to 15 November 2013 05:34:59 JST) of ambient noise at each station. The noise is band pass (1.0 to 10.0 Hz) filtered and added to the synthetic waveforms generated
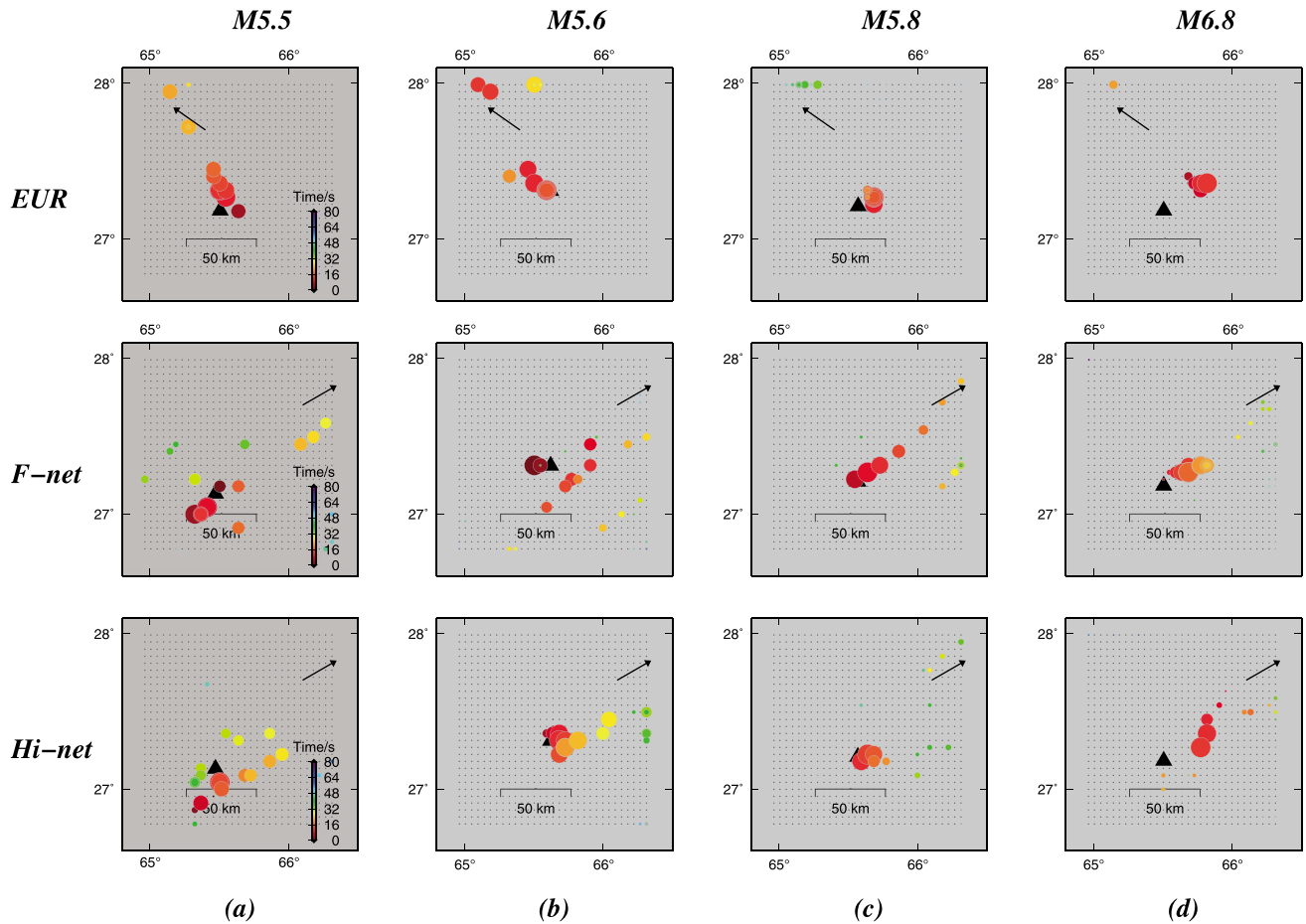

Figure 5. Backprojection results for aftershocks ((a–d) *M* 5.5 to *M* 6.8) using station corrections derived from the main shock for the European array, F-net, and Hi-net.
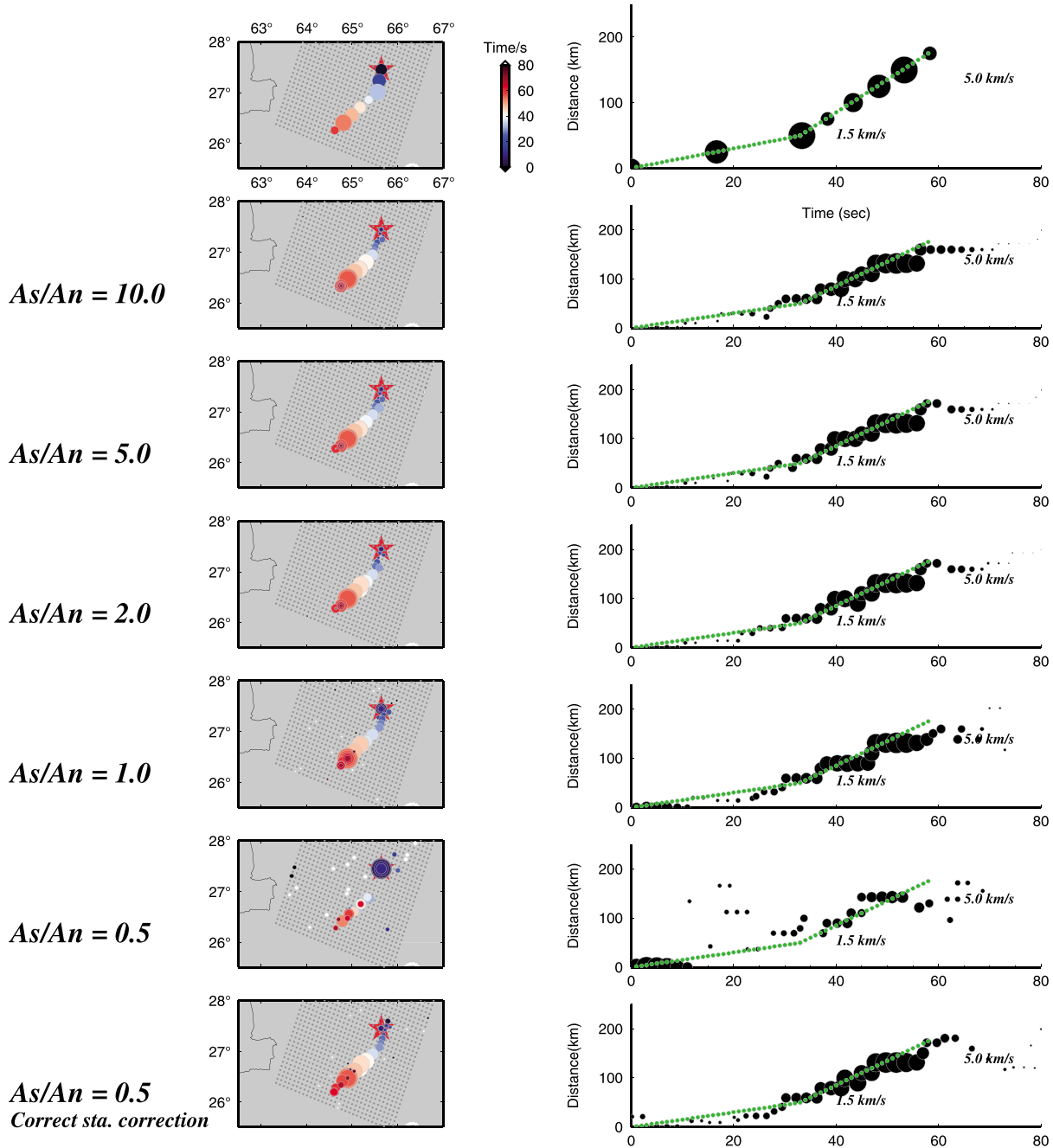
Figure 6. Location, timing, and amplitude for the stack with the maximum stacked amplitude at each time step (1 s) for backprojection of synthetic waveforms with different noise levels. Top trace is the input model which uses eight point sources with varying seismic moments and depths distributed every 30 km along a fault plane that is similar to surface scarps of the 24 September 2013 M_W 7.7 Pakistan earthquake. The results for five different signal-to-noise ratios from 10.0 to 0.5 are shown in (left column) map view and (right column) time-distance plots. The bottom panels show the results for a signal-to-noise ratio of 0.5, but station corrections were calculated using low-noise data.

for the scenario described above. The level of the noise is adjusted so that the amplitude ratio, As/An, between the signal (synthetic) and noise had various values of 10 to 0.5.

Similar to the procedure used in the actual data analyses, we align the first 10 s of the waveforms, and the backprojection procedure is carried out on the waveforms, with the same window lengths and offsets used in this study. For As/An greater than or equal to 1.0, the rupture speeds and locations can be resolved very well, even for the slow beginning (Figure 6). When As/An drops to 0.5, the backprojection procedure cannot resolve the
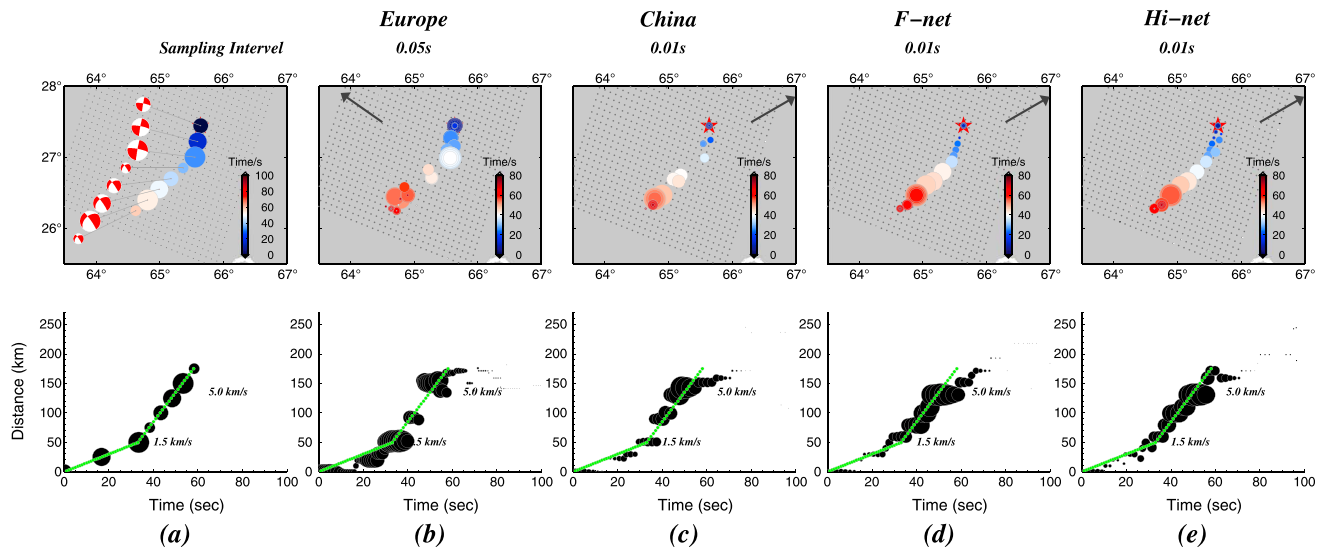
Figure 7. Results of the numerical tests for the four arrays using a synthetic source with eight point sources and varying rupture speed of 1.5 and 5.0 km/s. (a) Input model is shown. Results of the backprojection in (top row) map view and (bottom row) time-distance plots are shown for (b–e) the four arrays. Array names are indicated at the top. In Figure 7 (bottom row), model rupture velocities (1.5/5.0 km/s) are indicated by green lines.

locations and timing of the sources. It is noted that the problem for high noise levels is that the station corrections cannot be correctly resolved. For example, if we use the previously determined station corrections, using signal levels smaller than the noise (As/An = 0.5), the backprojection procedure can still correctly resolve the rupture speeds (see bottom panel of Figure 6). The signal-to-noise ratio for typical data used in this study is higher than 5.

Figure 7 shows the results of this numerical test for the four arrays with background noise of As/An = 5. Both the rupture pattern and the rupture speed are recovered very well for the seismograms generated by the four arrays, though there seems to be a slightly larger distortion for the European data, probably due to the relatively lower sampling rate and/or the differences in the waveforms shapes caused by locations of the stations that are on either side of the nodal plane (Figure 2).

4. Global Observation

Simple alignment of teleseismic *P* wave recordings can show raw image of the spatiotemporal slip distribution and rupture direction [e.g., *Fan and Shearer*, 2015]. To confirm the general features of the rupture (i.e., rupture propagation direction), we show globally recorded vertical broadband seismic velocity waveforms for distances of 30° to 100°, filtered between 0.01 and 0.5 Hz and ordered by azimuth. The waveforms are aligned on the initial arrivals which were picked manually (Figure 8).

We pick the first large pulse that can be easily seen over all azimuths, as shown by the red dots in Figure 8. A relative location method [*Wang and Mori*, 2012] is used to locate the source of the pulse. The source of the pulse is located 71 km southwest of the epicenter at around 20 s after the origin time, similar to the backprojection results derived from the three broadband arrays, which shows source locations about 50–70 km southwest of the epicenter. The green dots in Figure 8b show predicted arrivals for the estimated pulse.

Notice that there are closely spaced small pulses in the first 10 s of the global data that can be seen in all azimuths without much moveout, suggesting a slow rupture propagation for the beginning few seconds. This is consistent with the slow rupture propagation observed in our and others' backprojection results [*Avouac et al.*, 2014]. The transition from slower to faster rupture speed has also been seen in several other strike-slip earthquakes, for example, the 2001 Kunlun *M* 7.8 earthquake [*Vallée et al.*, 2008; *Walker and Shearer*, 2009].

5. Comparison With Surface Faulting

The observed extensive surface faulting provides a unique opportunity for directly comparing the backprojection results with the high-resolution geodetic results on a relatively simple fault. Previous studies
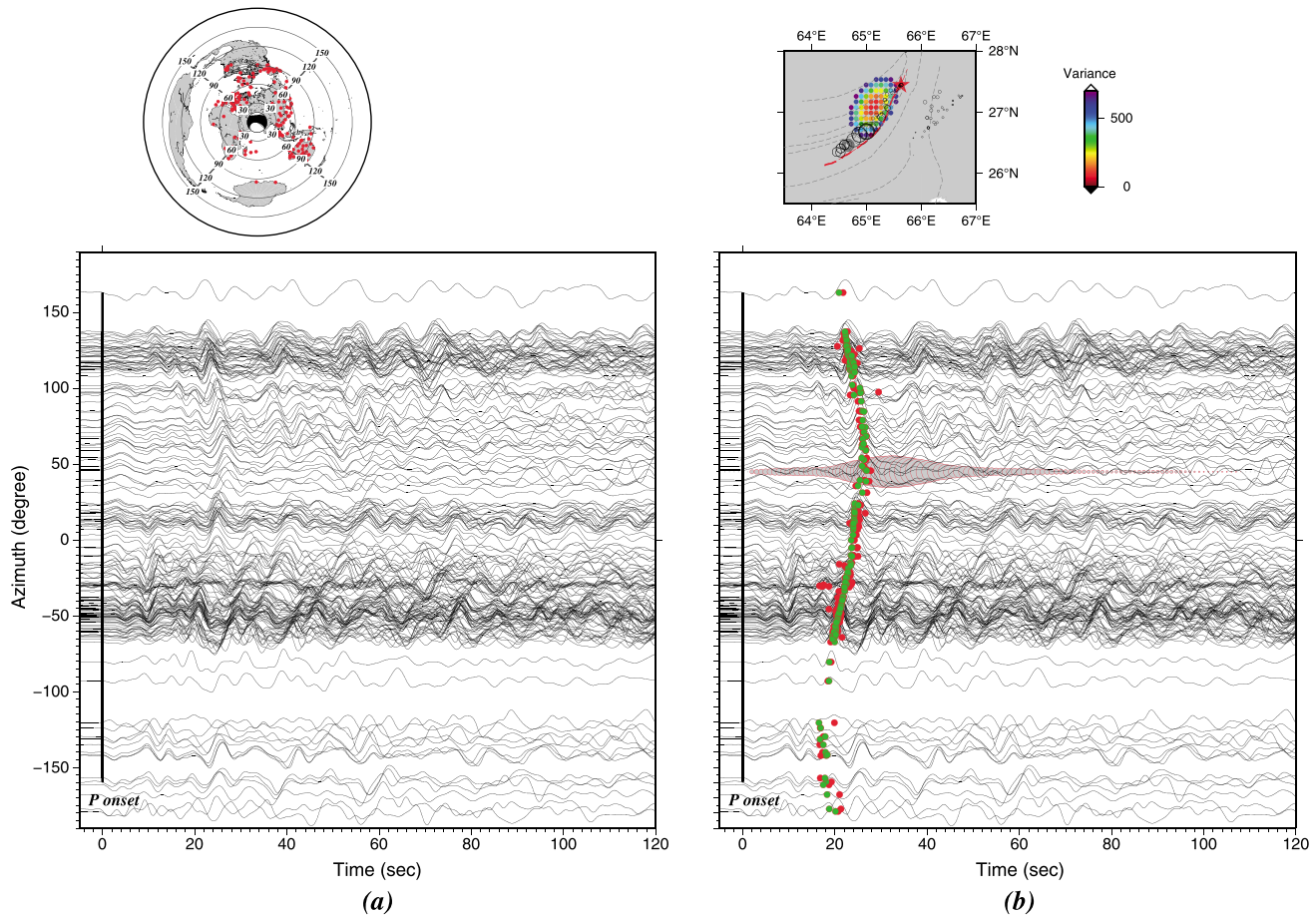
Figure 8. (a) Vertical broadband seismograms from global networks for distance of 30° to 100° are aligned on the *P* onset and sorted by azimuth. The waveforms are filtered between 0.01 and 0.5 Hz. (b) Top figure shows the calculated location (area with red dots) for the first large pulse using the arrival times shown by the red dots on the seismograms. The black circles indicate the locations of points with maximum amplitude in each time window derived from the Hi-net data filtered between 0.5 and 2.0 Hz. The green dots on the seismograms are the predicted arrival from the forward calculation using the determined pulse location. The size and azimuth of the gray circles (bottom right) indicate the maximum amplitude in each time window derived from backprojecting Hi-net data.

[*Ishii et al.*, 2007; *Wang and Mori*, 2011b; *Yao et al.*, 2012; *Fukahata et al.*, 2014] indicate that backprojection methods can recover the synthetic subevents and aftershocks well. The effects of complicated structure beneath seismic arrays and in the source area have not been investigated fully. Geodetic results, especially the optical image in this case, provide high-resolution surface deformation data and are thus capable of being a reference for a realistic test of the backprojection resolution.
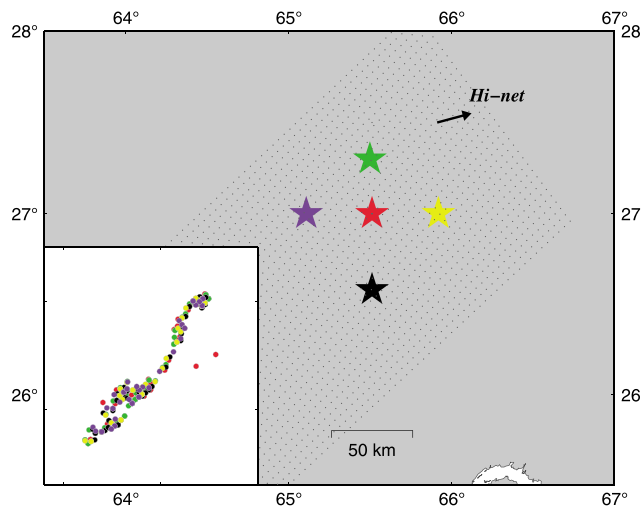
The shape of the trace of the rupture propagation derived from the Hi-net data appears to be very similar to the curved shape of the surface displacements of the fault (Figure 9a) [*Avouac et al.*, 2014; *Barnhart et al.*, 2014; *Jolivet et al.*, 2014; *Yague-Martinez et al.*, 2014; *Zinke et al.*, 2014], although there is a significant spatial offset. To check if the curved shape of the trace derived from the backprojection varies with different locations of the epicenter, we shift the assumed initiation point 40 km to north, east, south, and west from the USGS epicenter and then back project the waveforms using the shifted epicenters. The shapes of the rupture traces from the backprojection do not change significantly, indicating that the relative locations of the sources derived from the backprojection are not largely affected by the absolute epicenter location (Figure 10). This test shows that the backprojection determines the relative locations of the sources of radiated energy with reference to the epicenter, and the velocity heterogeneities in the source region do not significantly affect the results.

The optical image study of the surface fault provides a high-resolution estimate of the absolute location of the surface deformation with uncertainties less than a few hundred meters [*Leprince et al.*, 2007]. These results are compared with our backprojection results. Since the fault plane is subvertical around the epicenter
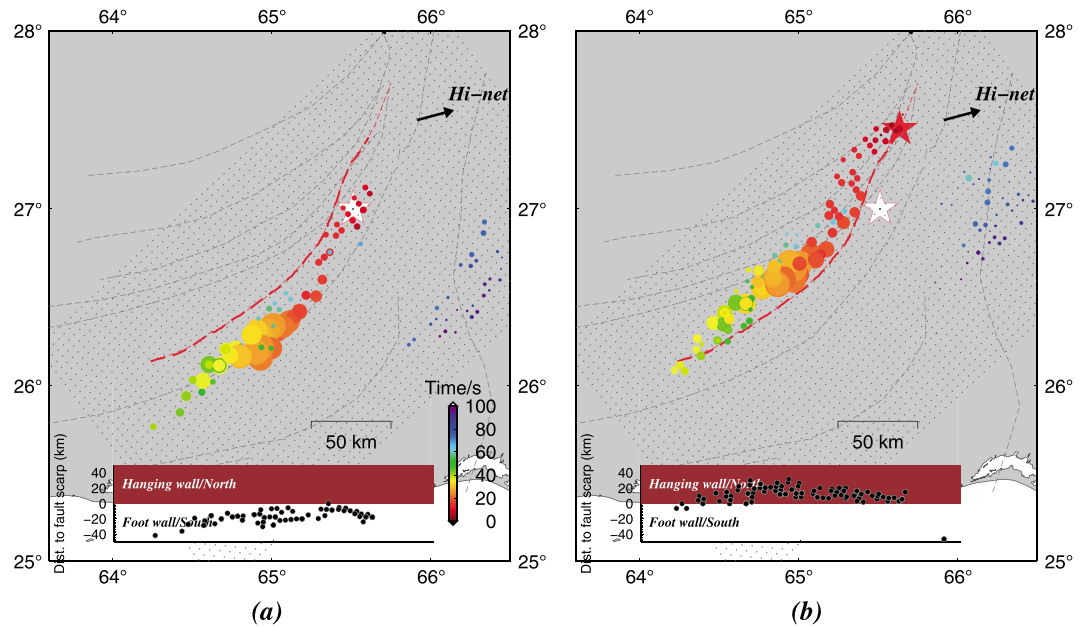
Figure 9. Location, timing, and amplitude for the stack with the maximum correlation at each time step (1 s) derived from Hi-net data filtered in several high-frequency bands (band-pass-filtered from 0.5 to 2.0 Hz, 0.8 to 8.0 Hz, and 1.0 to 10.0 Hz). Gray grid points indicate the tested source locations. Gray dashed lines show the preexisting geological faults [*Lawrence et al.*, 1981]. The thick red dashed lines indicate the surface trace caused by this earthquake, and deduced fault trace is shown by the thin red dashed line [*Avouac et al.*, 2014]. Inset shows the minimum distance from the maximum points to the surface scarps. (a) The results assuming the USGS epicenter. (b) The results for an epicenter shifted 40–50 km to the northeast which is based on the best fit of the shape of results of the backprojection and geodetic study [*Avouac et al.*, 2014].
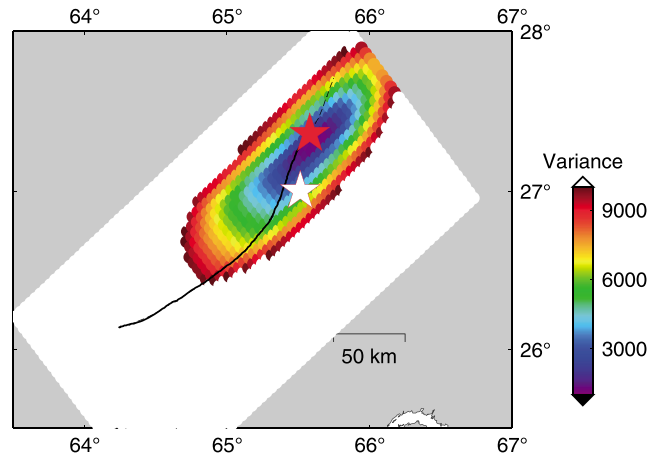
and the main slip is concentrated in the top 10 km with limited displacement on the underlying décollement [*Jolivet et al.*, 2014], the location of the high-frequency emissions should be similar to the surface trace of the rupture. To find the best fitting epicenter, we test a grid of 71×41 points spaced at 5 km in the source area for the assumed initiation of the backprojection and calculate the summed distances between the backprojected sources and the surface scarp derived from the optical images. The distance is calculated from the maximum amplitude points to the closest point on the surface scarp. Comparing the summed offsets between the surface scarp and the sources determined by the backprojection, we find that the best fit is obtained when the epicenter is set 40–50 km northeast of the USGS epicenter. The contoured values of the misfit are shown in Figure 11.

There is a west to northwest dip for the fault, especially in the southern region [e.g., *Jolivet et al.*, 2014], so we would expect that the seismic sources at depth would locate 5 to 15 km west and northwest of the surface trace. Since we do not have depth resolution in the backprojection analyses, we cannot make


Figure 10. Stacked locations for the maximum correlation at each time step (1 s) derived from Hi-net data filtered between 1.0 and 10.0 Hz with different epicenters. Here the red star indicates the epicenter determined by the USGS. The other four stars were shifted 40 km to the north, east, south, and west from the USGS epicenter. The results show that relative locations of the maximum points and the shape of the distribution do not change significantly for different epicenter locations (inset).

Figure 11. Calculated misfit between the surface scarps determined by optical images [*Avouac et al.*, 2014] and the source locations derived from the backprojection for each grid point used as an assumed epicenter. White and red stars indicate the original USGS and best fitting epicenters, respectively. The black solid line shows the surface scarp, and the black dashed line indicates the deduced surface scrap.

this correction, and there is probably an eastward bias to the inferred epicenter. Locations of high-frequency sources derived from the backprojection using this epicenter show a good correlation to the surface displacements derived from the optical image analysis. There is a similarity in the overall shape and a correlation of the locations of the large radiated energies with the large surface displacement (Figure 9b). The comparison between results derived from backprojection and geodetic study suggests that the relative location uncertainty from backprojection using Hi-net data can be 10–20 km or less.

Figure 12 shows the backprojection results for the four arrays using the calibrated epicenter. The shape of the high-frequency sources does not change significantly, compared to those in Figure 3.

6. Discussion

In this study we implemented a backprojection method to data recorded on European array, China array, F-net, and Hi-net to trace the rupture process of the 2013 Pakistan earthquake. The results show a general similarity with clear southwest rupture for a duration of about 40–50 s. The largest amplitudes for the high-frequency energy occur 20 to 50 s after the initiation and the direction of rupture changes more toward the west for the later part of the rupture.
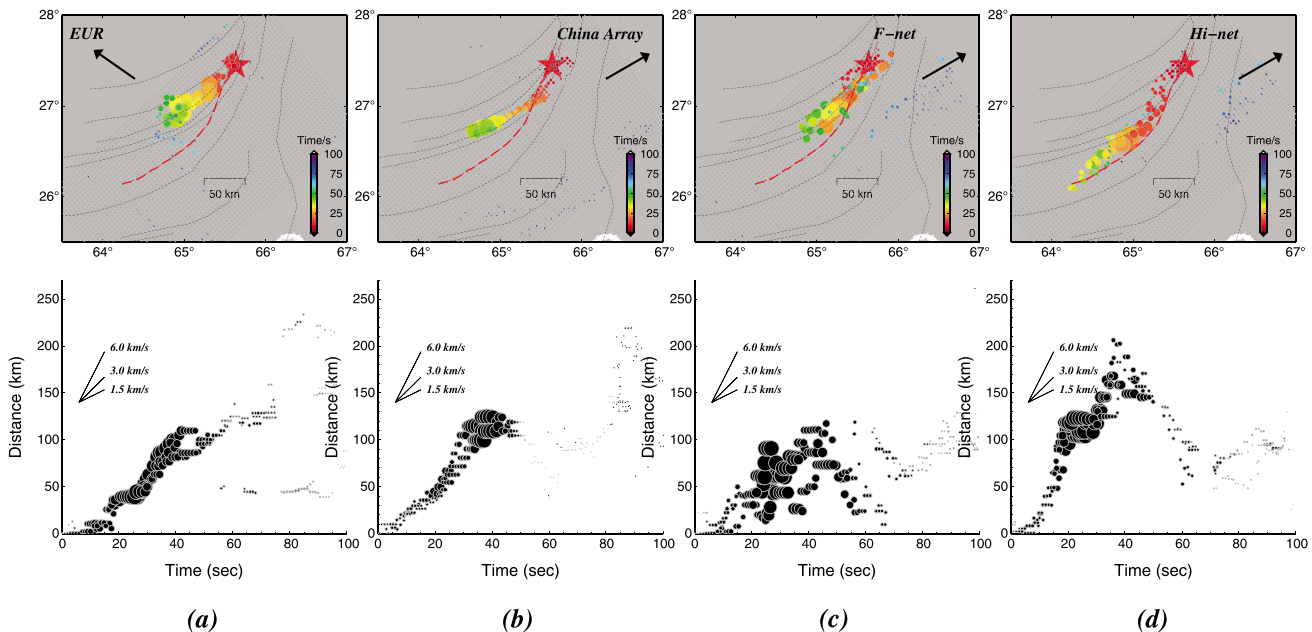
Figure 12. Same as Figure 3 except the calibrated epicenter (Figure 11) from comparison with the surface fault data is used instead of the USGS epicenter. The surface scarp [*Avouac et al.*, 2014] is shown by the red dashed line.
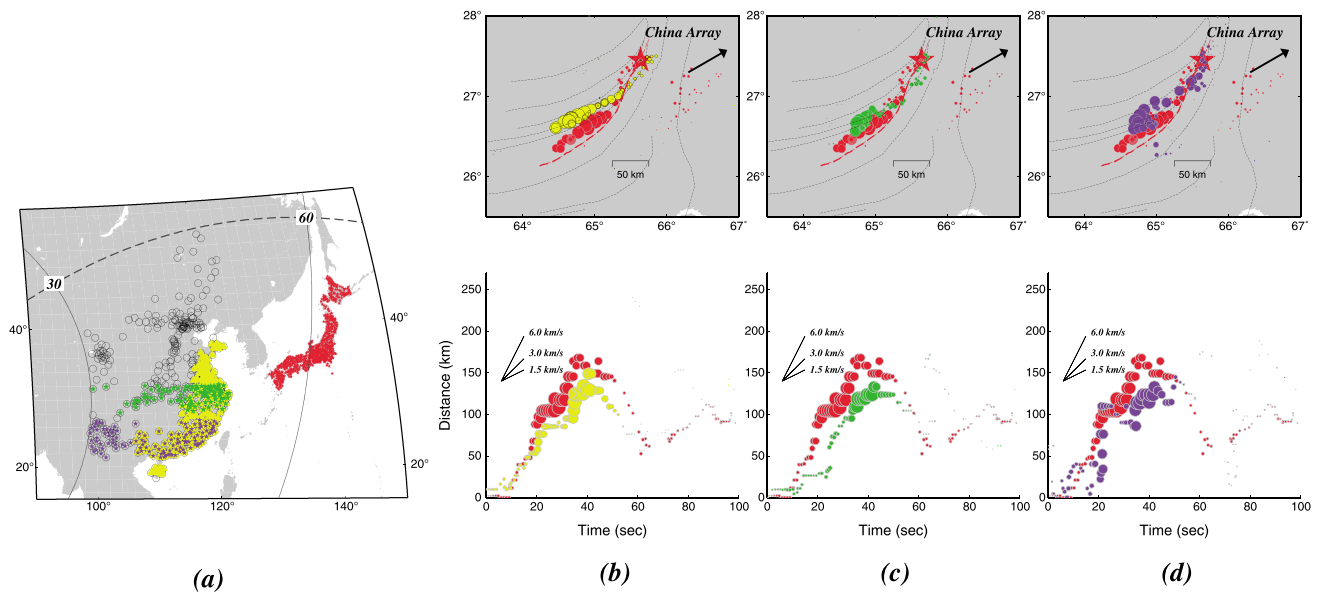
Figure 13. Comparison of results derived from data recorded at subsets of China array. (a) Distributions of three subsets of China array (yellow, green, and purple). The black circles indicate the whole stations of China array used in this study. The red star indicates the Hi-net stations. (b–d) The timing and amplitude for the stack with maximum stacked amplitude at each time step (1 s) (top row) in the map view and (bottom row) in time-distance plots. Notice that results for the subsets of the China array are colored by yellow in Figure 13b, green in Figure 13c, and purple in Figure 13d, respectively. The results for the Hi-net are indicated by red circles for comparison.

One significant difference among the results from the four arrays is that the Hi-net data show a longer rupture length of about 150–180 km, compared to 120 to 140 km for the China array. The various bootstrap and numerical tests in section 3 do not show significantly different resolution for Hi-net and China array. To further investigate this difference, we back project data (band-pass-filtered between 0.5 and 2.0 Hz) recorded at China array using a Japan-sized and Japan-shaped subset of dense stations in the East China (Figure 13a). The results show a similar source trace to those of derived from Hi-net data, although there is still 15–25 km difference at the southwest end of the rupture that is comparable to the location uncertainties illustrated at the resolution tests. Also, the results derived from the subset of China data show clear fast rupture propagation after 10 s, which is consistent with the rupture speed history deduced from the Hi-net data. We back project another two subsets of China data using ~100 stations with geometries roughly perpendicular to Hi-net. The results show shorter rupture lengths of 120–130 km and a lower rupture speed of 3.0 km/s, although the fast rupture segment (~4.0 km/s) is ambiguously seen from 10 to 40 s (Figure 13). From this analysis and the resolution tests, we suppose that the differences in rupture length and rupture speed among the four regional arrays might be due to the different resolutions affected by array geometry, number of stations, and/or location in the focal sphere. Especially, the results derived from three subsets of China data indicate that the array geometry largely affects the final images of backprojection, thus requiring further investigations and careful considerations in future studies.

From the Hi-net and China data, we obtained an average rupture speed of 3.7–4.1 km/s (Figure 13b), which is probably close to or faster than local shear wave velocity of 3.6–3.7 km/s at depth of 12–26 km [*Laske et al.*, 2001]. The supershear rupture speed we observed for the Hi-net and China data might be one of the first examples on a curved fault. Previous earthquake examples [e.g., *Bouchon et al.*, 2010] and theoretical studies [e.g., *Das and Aki*, 1977; *Zhang and Chen*, 2006] have attributed very fast rupture speed to long and straight segments of faults.

7. Conclusions

We compared the backprojection results for the 2013 Pakistan earthquake using four independent arrays in Europe, China, and Japan (F-net and Hi-net). The general features of the results are similarly showing a rupture propagation toward the southwest for duration of about 40–50 s. Bootstrap tests show the resolution for the various arrays. F-net in Japan has the poorest quality because of the small number of stations. The

European array also has less resolution than the China array and Hi-net in Japan. This may be attributed to the fact that the *P* wave arrivals in Europe had takeoff angles close to one of the nodal planes. The China array and Hi-net had the best resolution for studying this earthquake. From the Hi-net data and a subset of China data, we observed a fast rupture speed of 3.7–4.1 km/s, which is probably close or faster than the local shear wave velocity.

References

Ambraseys, N., and R. Bilham (2003), Earthquakes in Afghanistan, *Seismol. Res. Lett.*, *74*, 107–123.

Avouac, J.-P., F. Ayoub, S. Wei, J.-P. Ampuero, L. Meng, S. Leprince, R. Jolivet, Z. Duputel, and D. Helmberger (2014), The 2013, M_w 7.7 Balochistan earthquake, energetic strike-slip reactivation of a thrust fault, *Earth Planet. Sci. Lett.*, *391*, 128–134.

Barnhart, W., G. Hayes, R. Briggs, R. Gold, and R. Bilham (2014), Ball-and-socket tectonic rotation during the 2013 M_w7. 7 Balochistan earthquake, *Earth Planet. Sci. Lett.*, *403*, 210–216.

Bouchon, M., H. Karabulut, M.-P. Bouin, J. Schmittbuhl, M. Vallée, R. Archuleta, S. Das, F. Renard, and D. Marsan (2010), Faulting characteristics of supershear earthquakes, *Tectonophysics*, *493*, 244–253.

Byrne, D. E., L. R. Sykes, and D. M. Davis (1992), Great thrust earthquakes and aseismic slip along the plate boundary of the Makran subduction zone, *J. Geophys. Res.*, *97*, 449–478, doi:10.1029/91JB02165.

Das, S., and K. Aki (1977), A numerical study of two-dimensional spontaneous rupture propagation, *Geophys. J. Int.*, *50*, 643–668.

Efron, B. (1979), Bootstrap methods: Another look at the jackknife, *Ann. Stat.*, 1–26.

Fan, W., and P. M. Shearer (2015), Detailed rupture imaging of the 25 April 2015 Nepal earthquake using teleseismic *P* waves, *Geophys. Res. Lett.*, *42*, 5744–5752, doi:10.1002/2015GL064587.

Fukahata, Y., Y. Yagi, and L. Rivera (2014), Theoretical relationship between back-projection imaging and classical linear inverse solutions, *Geophys. J. Int.*, *196*, 552–559.

Heidarzadeh, M., and K. Satake (2014), Possible sources of the tsunami observed in the northwestern Indian Ocean following the 2013 September 24 M_w 7.7 Pakistan inland earthquake, *Geophys. J. Int.*, *199*, 752–766.

Ide, S. (2002), Estimation of radiated energy of finite-source earthquake models, *Bull. Seismol. Soc. Am.*, *92*, 2994–3005.

Ishii, M. (2011), High-frequency rupture properties of the M_w 9.0 off the Pacific coast of Tohoku earthquake, *Earth Planets Space*, *63*, 609–614.

Ishii, M., P. M. Shearer, H. Houston, and J. E. Vidale (2005), Extent, duration and speed of the 2004 Sumatra-Andaman earthquake imaged by the Hi-Net array [in English], *Nature*, *435*, 933–936, doi:10.1038/Nature03675.

Ishii, M., P. M. Shearer, H. Houston, and J. E. Vidale (2007), Teleseismic *P* wave imaging of the 26 December 2004 Sumatra-Andaman and 28 March 2005 Sumatra earthquake ruptures using the Hi-net array, *J. Geophys. Res.*, *112*, B11307, doi:10.1029/2006JB004700.

Ishii, M., E. Kiser, and E. L. Geist (2013), M_w 8.6 Sumatran earthquake of 11 April 2012: Rare seaward expression of oblique subduction, *Geology*, *41*, 319–322.

Jolivet, R., Z. Duputel, B. Riel, M. Simons, L. Rivera, S. Minson, H. Zhang, M. Aivazis, F. Ayoub, and S. Leprince (2014), The 2013 M_w 7.7 Balochistan earthquake: Seismic potential of an accretionary wedge, *Bull. Seismol. Soc. Am.*, *104*, 1020–1030.

Kennett, B., and E. Engdahl (1991), Traveltimes for global earthquake location and phase identification, *Geophys. J. Int.*, *105*, 429–465.

Kennett, B., A. Gorbatov, and S. Spiliopoulos (2014), Tracking high-frequency seismic source evolution: 2004 M_w 8.1 Macquarie event, *Geophys. Res. Lett.*, *41*, 1187–1193, doi:10.1002/2013GL058935.

Kiser, E., and M. Ishii (2011), The 2010 M_w 8.8 Chile earthquake: Triggering on multiple segments and frequency-dependent rupture behavior, *Geophys. Res. Lett.*, *38*, L07301, doi:10.1029/2011GL047140.

Koper, K. D., A. R. Hutko, T. Lay, and O. Sufri (2012), Imaging short-period seismic radiation from the 27 February 2010 Chile (M_W 8.8) earthquake by back-projection of *P*, *PP*, and *PKIKP* waves, *J. Geophys. Res.*, *117*, B02308, doi:10.1029/2011JB008576.

Kruger, F., and M. Ohrnberger (2005), Tracking the rupture of the M_w = 9.3 Sumatra earthquake over 1,150 km at teleseismic distance, *Nature*, *435*, 937–939, doi:10.1038/Nature03696.

Laske, G., G. Masters, and C. Reif (2001), *CRUST 2.0: A New Global Crustal Model at 2× 2 Degrees*, *Inst. Geophys. Planet. Phys.*, The Univ. of Calif., San Diego, Calif. [Avaialble at http://mahi.ucsd.edu/Gabi/rem.dir/crust/crust2.html.]

Lawrence, R., R. Yeats, S. Khan, A. Farah, and K. DeJong (1981), Thrust and strike slip fault interaction along the Chaman transform zone, Pakistan, *Geol. Soc. London, Spec. Publ.*, *9*, 363–370.

Leprince, S., S. Barbot, F. Ayoub, and J.-P. Avouac (2007), Automatic and precise orthorectification, coregistration, and subpixel correlation of satellite images, application to ground deformation measurements, *IEEE Trans. Geosci. Remote Sens.*, *45*, 1529–1558.

Meng, L., J.-P. Ampuero, J. Stock, Z. Duputel, Y. Luo, and V. Tsai (2012), Earthquake in a maze: Compressional rupture branching during the 2012 M_w 8.6 Sumatra earthquake, *Science*, *337*, 724–726.

Ni, S., H. Kanamori, and D. Helmberger (2005), Seismology: Energy radiation from the Sumatra earthquake, *Nature*, *434*, 582–582.

Okada, Y., K. Kasahara, S. Hori, K. Obara, S. Sekiguchi, H. Fujiwara, and A. Yamamoto (2004), Recent progress of seismic observation networks in Japan-Hi-net, F-net, K-NET and KiK-net, *Earth Planets Space*, *56*, 15–28.

Satriano, C., E. Kiraly, P. Bernard, and J. P. Vilotte (2012), The 2012 M_w 8.6 Sumatra earthquake: Evidence of westward sequential seismic ruptures associated to the reactivation of a N-S ocean fabric, *Geophys. Res. Lett.*, *39*, L15302, doi:10.1029/2012GL052387.

Spudich, P., and L. N. Frazer (1984), Use of ray theory to calculate high-frequency radiation from earthquake sources having spatially variable rupture velocity and stress drop, *Bull. Seismol. Soc. Am.*, *74*, 2061–2082.

Vallée, M., M. Landès, N. Shapiro, and Y. Klinger (2008), The 14 November 2001 Kokoxili (Tibet) earthquake: High-frequency seismic radiation originating from the transitions between sub-Rayleigh and supershear rupture velocity regimes, *J. Geophys. Res.*, *113*, B07305, doi:10.1029/2007JB005520.

Walker, K. T., and P. M. Shearer (2009), Illuminating the near-sonic rupture velocities of the intracontinental Kokoxili M_w 7.8 and Denali fault M_w 7.9 strike-slip earthquakes with global *P* wave back projection imaging, *J. Geophys. Res.*, *114*, B02304, doi:10.1029/2008JB005738.

Wang, D., and J. Mori (2011a), Rupture process of the 2011 off the Pacific coast of Tohoku earthquake (*M* (*w*) 9. 0) as imaged with back-projection of teleseismic *P* waves, *Earth Planets Space*, *63*, 603–607.

Wang, D., and J. Mori (2011b), Frequency-dependent energy radiation and fault coupling for the 2010 M_w8. 8 Maule, Chile, and 2011 M_w9. 0 Tohoku, Japan, earthquakes, *Geophys. Res. Lett.*, *38*, L22308, doi:10.1029/2011GL049652.

Wang, D., and J. Mori (2012), The 2010 Qinghai, China, earthquake: A moderate earthquake with supershear rupture, *Bull. Seismol. Soc. Am.*, *102*, 301–308.

Wang, D., J. Mori, and T. Uchide (2012), Supershear rupture on multiple faults for the M_w 8.6 Off Northern Sumatra, Indonesia earthquake of April 11, 2012, *Geophys. Res. Lett.*, 39, L21307, doi:10.1029/2012GL053622.

Wang, D., J. Mori, and K. Koketsu (2016), Fast rupture propagation for large strike-slip earthquakes, *Earth Planet. Sci. Lett.*, *440*, 115–126, doi:10.1016/j.epsl.2016.02.022.

Wessel, P., and W. H. Smith (1991), Free software helps map and display data, *Eos Trans. AGU*, *72*, 441–446, doi:10.1029/90EO00319.

Yague-Martinez, N., E. Fielding, M. Haghshenas-Haghighi, X. Y. Cong, M. Motagh, U. Steinbrecher, M. Eineder, and T. Fritz (2014), Ground displacement measurement of the 2013 *M*7. 7 and *M*6. 8 Balochistan earthquake with TerraSAR-X ScanSAR data, in *IEEE International on Geoscience and Remote Sensing Symposium (IGARSS)*, pp. 950–953 , IEEE, Quebec, Canada.

Yao, H., P. Gerstoft, P. M. Shearer, and C. Mecklenbräuker (2011), Compressive sensing of the Tohoku-Oki M_w 9.0 earthquake: Frequency-dependent rupture modes, *Geophys. Res. Lett.*, *38*, L20310, doi:10.1029/2011GL049223.

Yao, H., P. M. Shearer, and P. Gerstoft (2012), Subevent location and rupture imaging using iterative backprojection for the 2011 Tohoku M_w 9.0 earthquake, *Geophys. J. Int.*, *190*, 1152–1168.

Yao, H., P. M. Shearer, and P. Gerstoft (2013), Compressive sensing of frequency-dependent seismic radiation from subduction zone megathrust ruptures, *Proc. Natl. Acad. Sci. U.S.A.*, *110*, 4512–4517.

Yue, H., T. Lay, and K. D. Koper (2012), En echelon and orthogonal fault ruptures of the 11 April 2012 great intraplate earthquakes, *Nature*, *490*, 245–249.

Zhang, H., and X. Chen (2006), Dynamic rupture on a planar fault in three-dimensional half-space—II. Validations and numerical experiments, *Geophys. J. Int.*, *167*, 917–932.

Zinke, R., J. Hollingsworth, and J. F. Dolan (2014), Surface slip and off-fault deformation patterns in the 2013 M_W 7.7 Balochistan, Pakistan earthquake: Implications for controls on the distribution of near-surface coseismic slip, *Geochem. Geophys. Geosyst.*, *15*, 5034–5050, doi:10.1002/2014GC005538.